Soft Matter

PAPER

View Article Online
View Journal

Cite this: DOI: 10.1039/d6sm00321d

Translational diffusion and isomerization reaction of a liquid crystal molecule at solid–liquid interface of ionic liquids studied by total internal reflection-transient grating spectroscopy

Masaki Fujiwara, [a] Hideaki Shirota, [b] Kento Kasahara, [c] Nobuyuki Matubayasi [c] and Yoshifumi Kimura *[a]

The translational diffusion coefficients and isomerization reaction rates of *N*-(4-methoxybenzylidene)-4-butylaniline (MBBA) dissolved in ionic liquids (ILs) were measured at the sapphire interface using total internal reflection-transient grating (TIR-TG) spectroscopy. 1-Alkyl-3-methylimidazolium bis(trifluoromethylsulfonyl)amides ($[C_n\text{mim}][NTf_2]$) were used as ILs with different alkyl chain lengths. The diffusion coefficient of MBBA in the bulk did not monotonically decrease with an increase in the solvent viscosity, and it was maximum in $[C_6\text{mim}][NTf_2]$. Based on the radial distribution functions (RDFs) calculated from molecular dynamics (MD) simulations, we interpreted that the non-monotonicity of diffusion was due to the fact that MBBA behaves as an amphiphilic surfactant at the interfaces between the polar and nonpolar domains of the ILs and diffuses selectively along the surfaces of the nonpolar domains. At the sapphire interface, the diffusion coefficient of MBBA was almost the same as that in the bulk, whereas the isomerization reaction rate was significantly accelerated, irrespective of the alkyl chain length. The contact angle measurement revealed that MBBA was significantly concentrated near the sapphire interface. The above experimental results were discussed in relation to the bulk and interfacial structures of ionic-liquid solutions of a liquid crystal molecule.

Received 11th April 2026,
Accepted 15th May 2026

DOI: 10.1039/d6sm00321d

rsc.li/soft-matter-journal

1. Introduction

Ionic liquids (ILs), defined as salts composed of cations and anions with melting points lower than 100 °C, show nanoscale phase separation into polar and nonpolar domains in the bulk phase when the alkyl chains attached to ions are long.[1–3] Owing to the heterogeneous structure, the diffusion dynamics of solute molecules show unique behaviour in ILs.[4–7] For example, the diffusion of carbon monoxide (CO) is much faster than predicted by the conventional Stokes–Einstein theory in 1-alkyl-3-methylimidazolium bis(trifluoromethylsulfonyl)amide ($[C_n\text{mim}][NTf_2]$). Furthermore, the deviation from the prediction becomes larger as the alkyl chain length of the cation increases.[6] However, the elongation of the alkyl chains per cation using dicationic ionic liquids, where two charged groups are connected by alkyl linkages, showed similar diffusion dynamics to those in the corresponding monocationic ILs without alkyl linkage chains.[8] Therefore, the diffusion dynamics are affected by the nanoscale construction.

In contrast to the heterogeneous bulk phase, ILs form layered structures at the interface, as indicated by experimental and computational studies.[3,9–12] At the air–IL surface of $[C_n\text{mim}][NTf_2]$, a monolayer structure with the nonpolar part protruding toward the surface was observed when the alkyl chain of the cation was short, whereas a double-layer structure was observed when the alkyl chain was long, as determined by sum-frequency generation (SFG) spectroscopy.[9] Our research group measured the thermal diffusivity at the air–IL surface of $[C_n\text{mim}][NTf_2]$ using interface-selective TG spectroscopy.[13] The results indicated that the thermal diffusivity at the surface was lower than that in the bulk phase when the alkyl chain of the cation was long, owing to the unique interfacial structure described above. A similar surface specific structure is found at the liquid–liquid interface of CCl_4, with fewer *gauche* defects than at the air–liquid interface owing to the solvophilic effect of CCl_4.[10] At electrode interfaces, multilayer structures composed of cations and anions have been suggested by X-ray and neutron reflectometry.[11,12] Although such interface specificity of diffusion is also expected for the translational diffusion of molecules at the interface, to

[a] *Graduate School of Science and Engineering, Doshisha University, Kyotanabe, Kyoto 610-0321, Japan. E-mail: yokimura@mail.doshisha.ac.jp*
[b] *Department of Chemistry, Chiba University, Inage, Chiba, 263-8522, Japan*
[c] *Graduate School of Engineering Science, The University of Osaka, Toyonaka, Osaka 560-8531, Japan*

the best of our knowledge, no direct measurements have been performed.

Liquid crystals (LCs) are mesophases between the solid and liquid states, having liquid-like fluidity and crystal-like anisotropy, and are basically composed of rod-shaped or disc-shaped molecules. The bulk structures of LCs are well understood and vary widely depending on the LC molecules, such as nematic, smectic, and columnar phases.[14–17] Owing to orientational anisotropy, several diffusion anisotropies in the LC phase have been observed.[18–20] For example, in the bulk of *N*-(4-methoxybenzylidene)-4-butylaniline (MBBA), the ratio of the self-diffusion coefficient parallel to the director $D_{\parallel}$ to that perpendicular to it $D_{\perp}$ is 1.3.[19] The diffusion anisotropy of the solute molecule methyl red in the nematic phase of 4-pentyl-4′-cyanobiphenyl (5CB) was also estimated to be $D_{\parallel}/D_{\perp}$ = 1.5 using forced Rayleigh scattering.[20] The interfacial structure of LCs has also been investigated.[21–23] For example, a smectic-like double layer forms at the surface of nematic 5CB, whereas surface-induced smectic multilayers with a much longer penetration depth form at the surface of smectic 4-octyl-4′-cyanobiphenyl (8CB).[22] Furthermore, atomic force microscopy (AFM) studies revealed that isotropic MBBA forms a smectic-like monolayer at the interface of silanated glass.[23] Diffusion coefficients at LC interfaces have been scarcely investigated. There is a study in which the diffusion coefficient of a fluorescent molecule, AlexaFluor 647, was measured at the interface between nematic 5CB and sapphire using single-molecule total internal reflection fluorescence microscopy.[24] This experiment revealed that the diffusion coefficient at the interface also exhibits anisotropy, and its degree is identical to that of the self-diffusion coefficient of 5CB in the bulk phase.

The physicochemical properties and structures of ionic-liquid solutions of a liquid crystal molecule are extremely intriguing: heterogeneous and/or oriented? However, to the best of our knowledge, previous research studies on the system are limited and have mostly focused on their thermal properties and optical anisotropy.[25–27] Dan *et al.* reported that when an Fe-based paramagnetic ionic liquid existed at several mol% in MBBA, the phase transition from nematic to isotropic changed from an entropic to an enthalpic activation barrier. The main cause of the conversion was interpreted as a decrease in the conformational entropy due to the suppression of out-of-plane distortions of the benzene rings of MBBA by the IL. As described above, the presence of ILs significantly affects LCs; therefore, it is expected that unique anomalies will also appear in the diffusion dynamics of LCs in ILs.

In this study, we investigated the translational diffusion and isomerization reaction of MBBA in imidazolium-based ILs with different alkyl chain lengths ([$C_n$mim][NTf_2]) using TG spectroscopy.[28] By total internal reflection (TIR) of the probe light, we evaluated the translational dynamics at the solid–liquid interface. The TG method has several advantages over conventional techniques for estimating diffusion coefficients, such as FCS, including high time-resolution, no requirement for fluorescent probes, straightforward signal interpretation, simultaneous estimation of diffusion coefficients and reaction rates, and ease of application at solid–liquid interfaces. The principle of the measurement is as follows: at first, interference fringes are generated by crossing two pump pulses within the sample solution. The molecules on the interference fringe undergo photoreactions to form a sinusoidal modulation of the refractive index change, which behaves as a diffraction grating. This modulation disappears due to molecular diffusion processes and thermal reactions. The diffusion coefficients and reaction rates can be evaluated by diffracting the probe beam and observing the time evolution of the diffracted light intensity (TG signal). In the case of interface-selective TG methods, diffracted light is generated from the evanescent wave caused by the TIR of the probe beam.[29–31] To reduce the constraints of TIR, sapphire, with a refractive index of 1.77, was used as the solid substrate because the critical angle of TIR depends on the difference in the refractive indices of the surface materials. In this system, the refractive index changes during the MBBA isomerization from the *trans*- to *cis*-form, behaving as a species grating, so that the TG signal indicates the diffusion of MBBA and the isomerization reaction rate. We found that the diffusion coefficient of MBBA in the bulk did not change monotonically with viscosity and reached a maximum value at a certain viscosity. In addition, the isomerization reaction of MBBA was anomalously accelerated at the sapphire interface. These anomalies are attributed to the unique structure of the ionic-liquid solutions of MBBA as will be discussed later.

2. Methods

2.1. Materials

[$C_n$mim][NTf_2] (n = 3, 4, 6, 8, 10, and 12; Scheme 1) was synthesized according to a previously reported method.[32] The purity of the anion (>typically 99.6%) was confirmed by ^{19}F NMR spectroscopy (JEOL, JNM-ECA300). MBBA (Scheme 2) was purchased from Sigma-Aldrich and used as received. After purifying the ILs by drying under vacuum at 60 °C for at least 12 hours, the ionic-liquid solutions of MBBA (20 mol%) were prepared by dissolving MBBA into the ILs for 10 min at 60 °C under vacuum. Hereafter, we abbreviate the solution of MBBA in [$C_n$mim][NTf_2] as IL_nLC. Although we attempted to prepare IL_2LC using the same procedure, MBBA did not completely dissolve into [C_2mim][NTf_2].

2.2. TG spectroscopy for the bulk

The experimental setup of the TG method for the bulk phase has been described elsewhere.[6] Briefly, the third harmonic output from a pulsed Nd:YAG laser (Continuum, Minilite, λ_{pump} = 355 nm) was used for the excitation pulse. The pulse

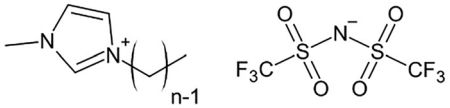

Scheme 1 Chemical formulas of $[C_n mim]^+$ and $[NTf_2]^-$.

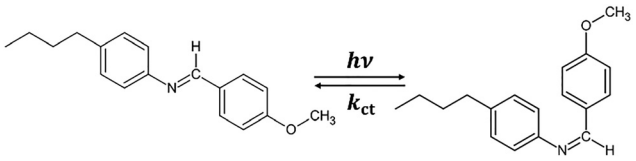

Scheme 2 Photoisomerization reaction of MBBA.

was split into two with a beam splitter and simultaneously introduced into the sample (the solution in a 1 cm path length quartz cell) at an angle θ. The continuous-wave (CW) output of a 633-nm He–Ne laser (LASOS, LGK-7654-8) was then introduced into the sample at a Bragg diffraction angle. The diffracted light (TG signal) was detected using a photomultiplier, transferred to an oscilloscope (Keysight Technologies, DSOX 2014A), and integrated over 2^5 times to reduce noise. The repetition frequency of the excitation pulse was 0.2 Hz. The grating wavenumber q was determined by the decay rate k_{th} of the thermal-grating signal from the bulk methanol solution of bromocresol purple using the following equation:

$$k_{th} = D_{th}q^2 \quad (1)$$

where D_{th} is the thermal diffusivity of methanol. All measurements were performed at room temperature (298 K).

2.3. Total internal reflection-TG (TIR-TG) spectroscopy for the interface

The experimental setup of the TIR-TG method for the solid–liquid interface was constructed referring to previously described methods.[29,31] The sample solution was poured inside an O-ring placed on an optical parallel and covered by a sapphire trapezoidal prism (Fig. 1). Two pump pulses (355 nm) were simultaneously introduced into the sample from the top. The TG signal was detected by diffraction of the CW output of a 642-nm diode laser (Spectra-Physics, Excelsior) introduced into the side of a sapphire prism to satisfy the TIR conditions (Fig. 1). Under the TIR conditions, the penetration depth of the probe beam, d_p, is given by the following equation:

$$d_p = \frac{\lambda_{probe}}{2\pi\sqrt{n_s^2 \sin^2\theta_i - n_l^2}} \quad (2)$$

where λ_{probe} is the wavelength of the probe beam, n_s and n_l are the refractive indices of the solid and liquid, respectively, and θ_i is the incident angle of the probe beam. In this work, the refractive index of the sapphire was $n_s = 1.77$, and the incident angle was $\theta_i = 76^\circ$. The amplitude of the probe beam decayed as

$$E = E_0 \exp\left(-\frac{z}{d_p}\right) \quad (3)$$

Considering that the intensity of the diffracted light is proportional to the probe beam intensity, the TIR-TG signal can monitor the averaged molecular dynamics from the interface to half of the penetration depth $d_p/2$. The TIR-TG signal was detected by a photomultiplier and transferred to an oscilloscope (Keysight Technologies, DSOX 2022A) and integrated more than 2^9 times to reduce noise. The repetition frequency of the excitation pulse was set to 0.2 Hz. The other measurement conditions were the same as those for the bulk samples. The water content of the sample solution was determined using Karl–Fischer titration (Kyoto Electronics Manufacturing Co. Ltd., MKC-501) after the TIR-TG measurement (Table S2).

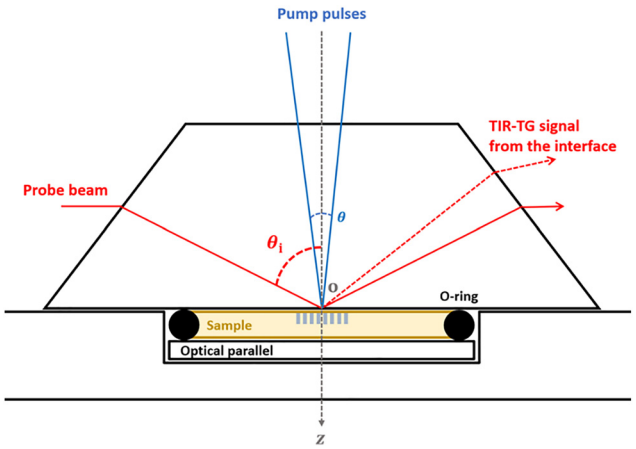

Fig. 1 Optical setup for the TIR-TG method.

2.4. Density, viscosity, refractive index, surface tension, and contact angle measurements

The density was measured using a densitometer (Anton Paar, DMA 4100M). Viscosity measurements were conducted using a DV-II + Pro (BROOKFIELD). The refractive index n_D was measured by an Abbe refractometer (Atago Co., Ltd, NAR-1T). The surface tension and contact angle on the sapphire were measured using a contact angle meter (Kyowa Interface Science, DMs-401), according to previously reported procedures for IL/solid interfaces.[33] The sapphire prism used for the TIR-TG measurements was used for the measurement. Prior to each contact angle measurement, the bottom surface of the sapphire prism was cleaned to remove contamination from droplets used in previous trials by wiping several times with anhydrous methanol, rinsing with the same solvent, and allowing the residual solvent to evaporate using an air blower. 10 droplets were measured for each sample, and then the values were averaged.

2.5. Molecular dynamics (MD) simulations

The structure of the IL$_n$LC (n = 4, 8, and 12) system was calculated using molecular dynamics (MD) simulations. The model of [C$_n$mim][NTf$_2$] developed by Lopes *et al.* was utilized[1] by scaling the charge to 0.8 times its original value. The structure of MBBA was optimized using Gaussian16[34] with the B3LYP functional and 6-31G(d) basis set. Then, it was converted to the OPLS-AA force field using the LigParGen webserver,[35–37] and the charges were rewritten to restrained electrostatic potential (RESP) charges[38] calculated by AmberTools.[39]

The initial structure was created using the Packmol package.[40] The IL_nLC was inserted into an isotropic box with a length of 10 nm to reproduce the experimental density (see Table S4 for details). MD simulations were performed using the GROMACS software.[41] The bond length was fixed using the LINCS algorithm, and the electrostatic interaction was calculated using the particle mesh Ewald (PME) method with a real-space cutoff radius of 1.2 nm. The same cutoff radius was used for Lennard-Jones interactions. First, the initial structure was energy-minimized and untangled for 100 ps in the NVT ensemble at 300 K. Second, after running for 5 ns in the NPT ensemble at 500 K, it was annealed to 298 K over 5 ns. Finally, equilibration was performed for 5 ns in the NPT ensemble at 298 K. The product run was simulated for 500 ns in the NPT ensemble using the V-rescale method for temperature control and the C-rescale method for pressure control, and the trajectory was recorded every 5 ps. We extracted the last 450 ns of the product run and calculated the radial distribution function (RDF) using the ANATRA package.[42] The diffusion coefficients were calculated from the mean square displacements (MSDs). Specifically, we divided the last 450 ns of the product run into 50 ns intervals, calculated the MSD for each interval, and determined the diffusion coefficient by fitting a straight line to the data between 10 ns and 20 ns at each interval.

3. Results

3.1. Physicochemical properties

The density and viscosity of IL_nLCs are listed in Table S1. With an increase in the alkyl chain length, the density decreased, and the viscosity increased monotonically. The tendency was consistent with the pure $[C_n\text{mim}][NTf_2]$, but the density of the IL_nLC was approximately 6.6% lower for n = 4, 4.4% lower for n = 8, and 3.7% lower for n = 12.[43] In contrast, the viscosity of the IL_nLC was approximately 27% higher for n = 4, 14% higher for n = 8, and 11% higher for n = 12 than that of the pure ILs.[44–46] The origins are discussed in Section 4.1. The refractive index n_D is listed in Table S2. From eqn (3), half of the penetration depth $d_p/2$ was 56 nm for IL_nLC (n = 4 and 8) and 58 nm for IL_{12}LC. The surface tension and contact angle on the sapphire are summarized in Table S3. As shown in Fig. 2, the contact angle decreased monotonically with the alkyl chain length.

3.2. TG signals from the bulk

The TG signals from the bulk were measured for all IL_nLCs. Fig. 3(A) shows a typical TG signal obtained from IL_4LC at q^2 = 1.4 μm^{-2}. The shapes of the TG signals were similar for all IL_nLCs. Under the assumptions that there is no significant difference in the diffusion coefficients of *trans*- and *cis*-form of MBBA and that no contribution of absorption at the probing wavelength, the TG signal was fitted by the following equation:[30]

$$I_{TG}(t) = \alpha[\delta n \exp(-k^{(b)}t)]^2 \quad (4)$$

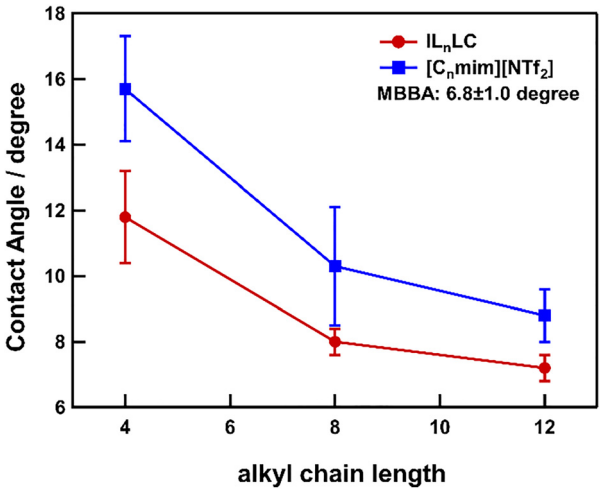

Fig. 2 Plots of the contact angle on the sapphire against the alkyl chain length.

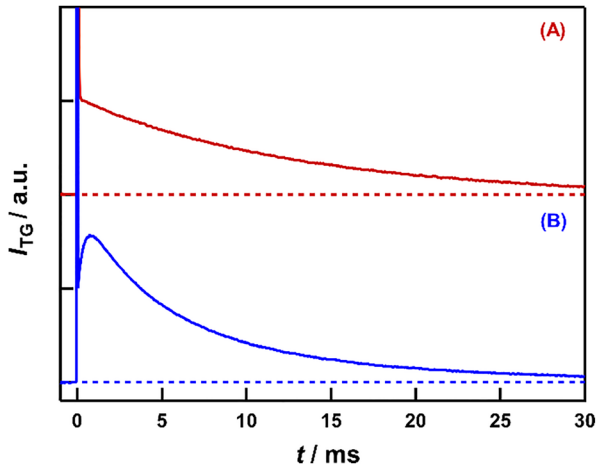

Fig. 3 Typical (A) TG signal at q^2 = 1.4 μm^{-2} and (B) TIR-TG signal at q^2 = 0.84 μm^{-2} from IL_4LC. The intensity of these signals is normalized at t = 0.25 ms.

where α is a proportional constant, δn is the refractive index change, and $k^{(b)}$ is the decay rate constant of species grating, respectively. The superscript (b) denotes the value in the bulk phase. The fitting accuracy was $k^{(b)}$ = 44.3 ± 0.1 s^{-1} for the signal in Fig. 3(A), as an example. By changing the crossing angle θ of the pump pulses, TG signals were obtained at various grating wavenumbers q^2 (= $4\pi \sin(\theta/2)/\lambda_{pump}$). The decay rate constants $k^{(b)}$ were plotted against q^2 (q^2 plot) as shown in Fig. 4 and Fig. S1. The decay of the TG signal was theoretically attributed to the diffusion and isomerization reaction of MBBA, and the diffusion coefficient was determined using the following relationship:

$$k^{(b)} = D^{(b)}q^2 + k_{ct}^{(b)} \quad (5)$$

where $D^{(b)}$ is the diffusion coefficient of MBBA and $k_{ct}^{(b)}$ is the isomerization reaction rate in Scheme 2, respectively. Since $k_{ct}^{(b)}$

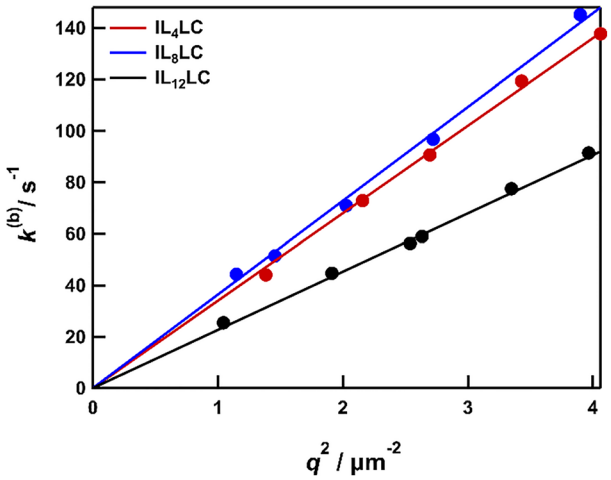

Fig. 4 Plots of the decay rate constants $k^{(b)}$ against q^2 for IL_nLC (n = 4, 8, and 12). Plots for the other IL_nLCs (n = 3, 6, and 10) are shown in Fig. S1.

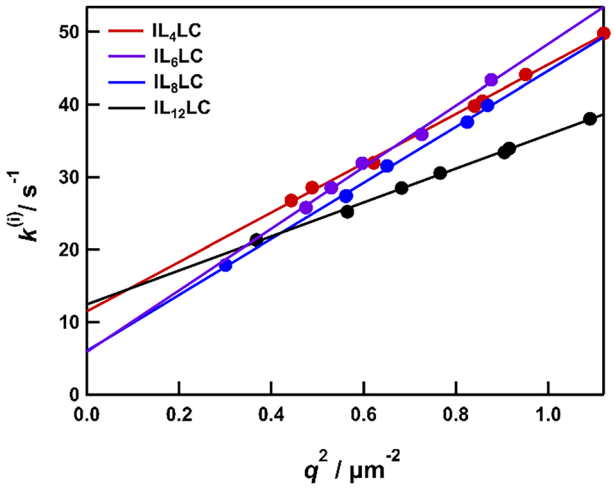

Fig. 5 Plots of the decay rate constants $k^{(i)}$ against q^2 for IL_nLC (n = 4, 6, 8, and 12).

is sufficiently small compared to the decay of the TG signal,[30] $k_{ct}^{(b)}$ was treated as zero. As shown in Table S1, the diffusion coefficient of MBBA did not decrease monotonically with the alkyl chain length and reached its maximum value in IL_6LC.

3.3. TIR-TG signals from the interface

The TIR-TG signals from the sapphire interface were measured for the IL_nLCs (n = 4, 6, 8, and 12). Fig. 3(B) shows the typical TIR-TG signal obtained from IL_4LC at $q^2 = 0.84$ μm^2. The shape of the TIR-TG signal was different from that of the TG signal, and the shapes were similar for the other IL_nLCs. The TIR-TG signal was simulated using the following equation:

$$I_{TG}(t) = \alpha[\delta n_f \exp(-k_f t) + \delta n_s \exp(-k_s t) + \delta n \exp(-k^{(i)} t)]^2 \quad (6)$$

where k_f and k_s are the additional decay rate constants, and $k^{(i)}$ is the decay rate constant corresponding to the diffusion component of MBBA, respectively. The superscript (i) denotes the value at the interface. The fitting accuracy was $k_f = (3.06 \pm 0.02) \times 10^3$ s^{-1}, $k_s = (1.72 \pm 0.01) \times 10^2$ s^{-1}, and $k^{(i)} = 39.8 \pm 0.2$ s^{-1} for the signal in Fig. 3(B), as an example. The q^2 plots of k_f and k_s are shown in Fig. S2 and S3. As shown in the figures, k_f and k_s were found to be independent of q^2. These components, independent of q^2, also appear when measuring solutes requiring consideration of back reactions, such as spiropyran and benzophenone.[7] Furthermore, similar ones have been reported at the interface between sapphire and organic solvents and have been interpreted as interface specific interactions between MBBA molecules.[30] Although the accurate assignments of k_f and k_s were unclear only from this measurement, since all observed components were fitted, the influence of these additional components onto $k^{(i)}$ was almost negligible.

The diffusion coefficient and the isomerization reaction rate at the interface were determined from the following relationship:[30]

$$k^{(i)} = D^{(i)} q^2 + k_{ct}^{(i)} \quad (7)$$

Fig. 5 shows the plot of $k^{(i)}$ against q^2. In contrast to the q^2 plot for the bulk phase, non-negligible interceptions appeared. This indicates that the isomerization of MBBA was accelerated at the sapphire interface. Table S2 summarizes the diffusion coefficient $D^{(i)}$ and reaction rate $k_{ct}^{(i)}$ obtained from eqn (7). Similarly to $D^{(b)}$, $D^{(i)}$ and $k_{ct}^{(i)}$ did not change monotonically with the alkyl chain length.

3.4. RDF calculated by MD simulations

The densities obtained from the MD simulations and their relative deviations from the experimental values are listed in Table S5. The simulated densities show good coincidence, although they are slightly higher than the real values. Fig. S4 shows the snapshots of MD simulations. Following the method reported by Lopes *et al.*, we color-coded the polar and nonpolar regions of the ILs (red and green, respectively).[1] MBBA is indicated in blue.

Fig. 6 shows the atom–atom RDFs based on the N atom on the Schiff base of MBBA with the N atom of the imidazolium ring attached to the methyl group, the terminal C atom of the cation, the N atom of the NTf_2 anion, and the N atom of MBBA itself. As shown in the figure, the RDFs between the N atoms showed no significant difference between the cations with different alkyl chain lengths. However, while no significant dependence was observed on the first peak of the RDF for the terminal C atom of the cation, the second peak appeared at approximately 9 Å as the alkyl chain length increased. Fig. 7 shows the atom–atom RDFs based on the terminal C atom of the butyl group of MBBA. The RDFs with the N atoms in the imidazolium ring and the N atom of the anion were not dependent on the alkyl chain length of the cation.

Table S6 shows the diffusion coefficients of MBBA, cations, and anions calculated from the MD simulations. It has been theoretically proved that the diffusion coefficient calculated from MD simulations is affected by the box size.[47] Therefore, Table S6 also shows the diffusion coefficients of MBBA

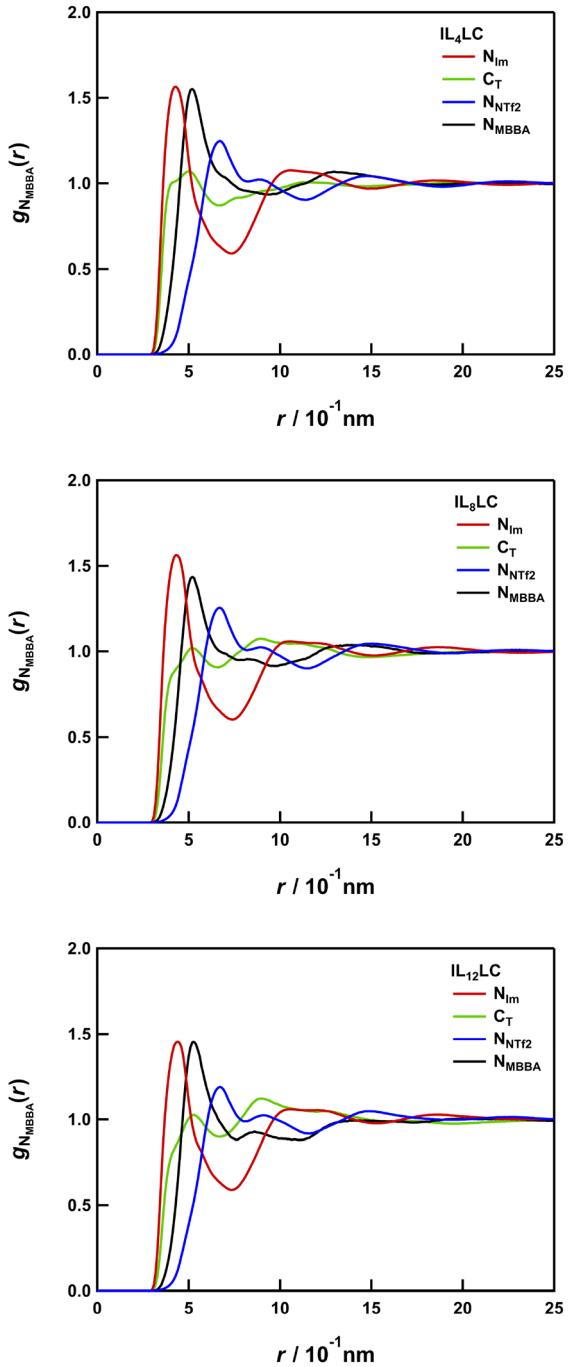

Fig. 6 Atom–atom RDFs based on the N atom of Schiff base of MBBA for the N atom of the imidazolium ring attached to the methyl group (N_{Im}), the terminal C atom of the alkyl chain on ILs (C_T), the N atom of the NTf_2 anion (N_{NTf2}), and the N atom of the Schiff base of MBBA (N_{MBBA}).

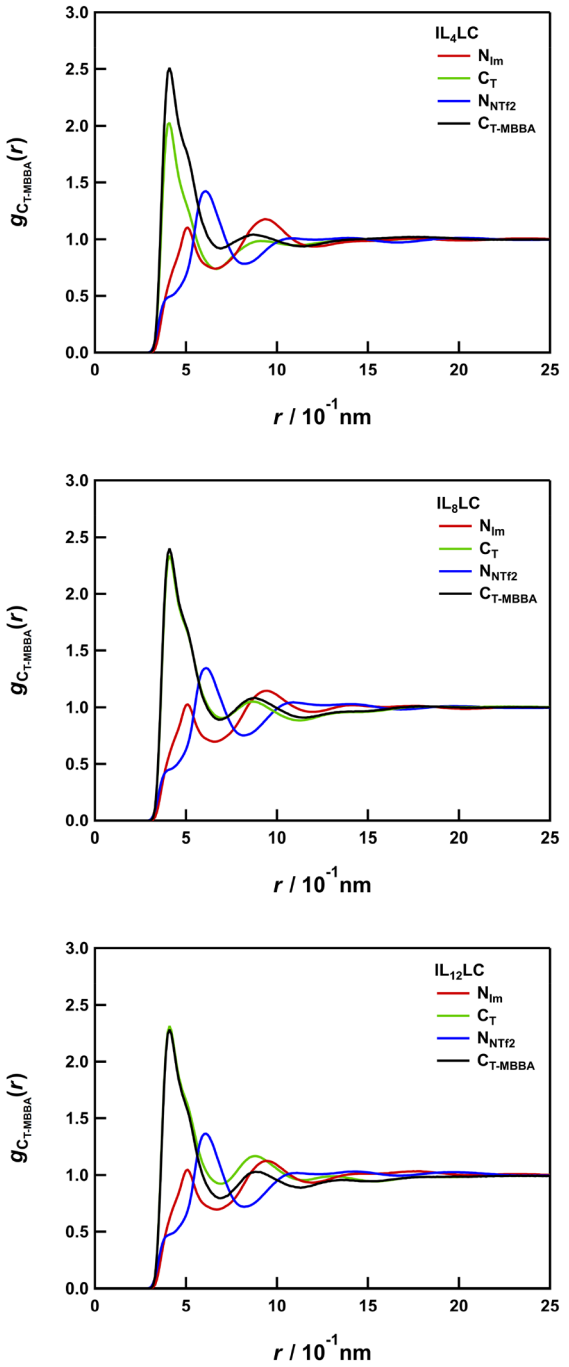

Fig. 7 Atom–atom RDFs based on the terminal C atom of the butyl chain on MBBA for the N atom of the imidazolium ring attached to the methyl group (N_{Im}), the terminal C atom of the alkyl chain on ILs (C_T), the N atom of the NTf_2 anion (N_{NTf2}), and the terminal C atom of the butyl chain on MBBA ($C_{T\text{-}MBBA}$).

corrected for the effect of box size using viscosity. The box size for each system was 9.75 nm for IL_4LC, 9.82 nm for IL_8LC, and 9.84 nm for $IL_{12}LC$. Viscosity values were approximated using experimental data. However, the corrected diffusion coefficient of MBBA was one order of magnitude smaller than the experimental values and did not reproduce the experimental trend.

4. Discussion

4.1. Correlation of diffusion coefficient with viscosity

First, we discuss the viscosity and density of the IL_nLC system. It has been reported that increases in the viscosity of pure ILs with elongation of the alkyl chain length are mainly due to van der Waals interactions, hydrogen bonding interactions,

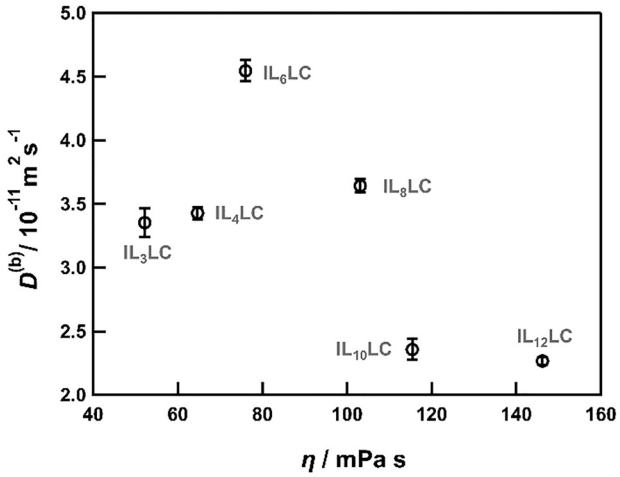

Fig. 8 Plots of $D^{(b)}$ against η for IL_nLC.

molecular weight, and chain tangling.[48,49] However, the viscosity of IL_nLC was higher than that of pure $[C_nmim][NTf_2]$, even though the molecular weight of MBBA (267.4 g mol^{-1}) is lower than that of $[C_3mim][NTf_2]$ (405.4 g mol^{-1}). This is probably due to the enhancement of the intermolecular interactions between ions and/or liquid crystals resulting from the addition of MBBA, a molecule with a dipole moment. On the other hand, the lower density of IL_nLC is mainly due to the fact that the density of MBBA (1.049 g cm^{-3}) is lower than that of the pure ILs; the alkyl chain dependence likely follows the same mechanism as in pure ILs, where packing efficiency decreases as the alkyl chain length increases.[43,49]

According to the Stokes–Einstein relation ($D = k_BT/C\pi r\eta$), the diffusion coefficient monotonically decreases with increasing viscosity η. Here k_B is the Boltzmann constant, T is the absolute temperature, C is the constant depending on the boundary constant, and r is the molecular radius, respectively. However, as shown in Fig. 8, $D^{(b)}$ showed a maximum value in IL_6LC. This non-monotonicity can be explained by the orientation of the MBBA molecules in ILs. As mentioned in the introduction, as the alkyl chain length of the cation increases, continuous polar and nonpolar domains develop in the bulk.[1] Because $[C_4mim][NTf_2]$ is almost a homogeneous solvent,[50] MBBA simply aggregates and homogeneously diffuses. However, as the alkyl chain length increased beyond that of a hexyl group, local domain structures are developed.[49] As shown in Fig. 6, because the RDFs between the N atom of MBBA and the N atoms of the imidazolium ring and of the NTf_2 anion did not depend on the alkyl chain length, the Schiff base and benzene ring of MBBA were selectively oriented toward the polar domain. Furthermore, because the RDFs between the terminal C atom of the MBBA butyl group and the terminal C atom of the cation are similar for IL_8LC and $IL_{12}LC$, the butyl group selectively dissolves in the nonpolar domain. In other words, MBBA orients at the interface between polar and nonpolar domains and behaves like an amphiphilic surfactant for these domains. Therefore, the faster diffusion of MBBA in IL_6LC than in IL_4LC is probably attributed to the selective diffusion of MBBA along surfaces on the polar domains. With alkyl chains longer than the hexyl group, the diffusion coefficient may have decreased owing to the viscosity. In addition, as shown in Fig. 6 and 7, the MBBA molecules are oriented such that their Schiff bases and terminal C atoms align with one another, similar to a liquid crystal. Hence, the fact that MBBA is dissolved at 20 mol% is one of the key points in understanding the behavior of the system.

The diffusion coefficient of MBBA calculated from the MD simulations, as shown in Table S6, did not reproduce the trend shown in Fig. 8. This discrepancy is probably due to an overestimation of solvent–solute or solute–solute interactions. It is known that force fields with fixed point charges in MD simulations tend to underestimate diffusivity in ionic liquids.[51] An improved treatment of electrostatic interactions that accounts for polarizability[52] may be essential to reproduce the experimentally observed trends, including quantitative agreement.

4.2. Comparison of diffusion coefficients at the interface and in the bulk

Fig. 9 shows the ratio of the diffusion coefficient at the interface to that in the bulk against alkyl chain length n. The ratio $D^{(i)}/D^{(b)}$ was almost 1.0, regardless of the alkyl chain lengths. The result may be attributed to the probing depth of the evanescent wave. As shown in eqn (2), the evanescent wave decays exponentially from the boundary (z = 0) in the normal direction. Therefore, since we evaluated the diffusion coefficient not only on the boundary but also slightly offshore, no significant difference could be observed between $D^{(i)}$ and $D^{(b)}$. In other words, the blurring of the interfacial nature of the diffusion coefficient was due to the limitations of the experimental method.

4.3. Acceleration of the reaction rate at the interface

The isomerization reaction rate $k_{ct}^{(i)}$ probed by TIR was larger than that in the bulk. Similar experimental results, in which reaction rates (*e.g.*, radical generation, fluorescence lifetime, and dimerization processes) accelerate at the interface, have also been reported in studies using spectroscopic techniques

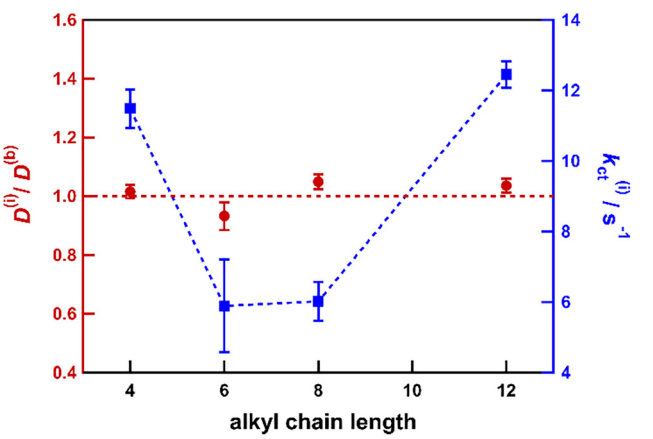

Fig. 9 Plots of $D^{(i)}/D^{(b)}$ (red) and $k_{ct}^{(i)}$ (blue) against alkyl chain length n of IL_nLC.

other than TIR-TG.[53–56] In all IL_nLCs measured by TIR-TG, the reaction rate accelerated at the interface, suggesting that the sapphire surface might catalyze the isomerization of MBBA. If the sapphire surface acts as a catalyst, the isomerization reaction should be accelerated in all solvents, including conventional organic solvents. However, Terazima's research group reported no acceleration of the MBBA reaction at the sapphire interfaces in acetonitrile, hexane, and acetone.[30] Therefore, we interpreted that the acceleration was attributed to the interfacial structure inherent to IL_nLC. Based on the results of the contact angle measurements, we can propose a rough picture of the interfacial structure. As shown in Fig. 2, the contact angle was significantly affected by the addition of MBBA, despite its molar ratio being only 20 mol%. Ignoring the nonlinear effects of mixing, the effective molar fraction of the contact angle, estimated from the angles of pure ILs and MBBA, was approximately 0.44 for IL_4LC, 0.66 for IL_8LC, and 0.80 for IL_{12}LC. That is, MBBA may be significantly concentrated near the sapphire interface; the longer the alkyl chain, the greater the effect. This is probably the main cause of acceleration. In other words, for IL_4LC, the interfacial structure is dominated by ILs, whereas for IL_{12}LC, it is dominated by MBBA, that is, the liquid crystal properties. The switching of the interface structure may appear as a non-monotonic acceleration, as shown in Fig. 9.

Although the specific interface structure is unclear only from the present measurement, AFM measurements revealed that isotropic MBBA strongly adsorbs onto silanated glass substrates and forms a monolayer-like smectic phase.[23] In addition, as mentioned in the introduction, ILs form ordered multilayer structures at the solid–liquid interface.[11,12] Hence, a similar ordered structure is expected at the sapphire interface of IL_nLC. Because the *cis*-form is bulkier and less orientable than the *trans*-form, the isomerization reaction rate is probably accelerated.

5. Conclusions

We investigated the translational diffusion and isomerization reaction of MBBA at the sapphire interface of IL_nLC using TIR-TG spectroscopy. In the bulk, the diffusion coefficient of MBBA did not monotonically decrease with increasing viscosity, reaching a maximum value in IL_6LC. We interpreted this non-monotonicity in diffusion as resulting from the fact that, based on the RDFs calculated from MD simulations, MBBA behaves as a surfactant at the interface between the polar and nonpolar domains of the ILs and diffuses selectively along the surface. The diffusion coefficient at the sapphire interface was almost the same as that in the bulk, which was due to probing the interfacial value using the evanescent wave. In contrast, the isomerization reaction rate at the sapphire interface was significantly accelerated. We interpreted that the acceleration was caused by the unique interfacial structure of IL_nLC and sapphire. The contact angle measurement suggested that MBBA was significantly concentrated near the sapphire interface. The present study of ionic-liquid solutions of a liquid crystal molecule will spice up solution chemistry.

In this study, the TIR-TG measurements were performed only at the sapphire interface; replacing the sapphire substrate with an electrode may significantly affect the isomerization reaction rate. As mentioned in the introduction, ILs form ionic multilayers at the electrode interface, and the structure is sensitive to the electrode potential. In addition, MBBA exhibits negative dielectric anisotropy, and its orientation changes when an electric field is applied to it. Therefore, it would be worthwhile from a physicochemical perspective to conduct the TIR-TG measurement at the IL_nLC/electrode interface.

Author contributions

M. F. performed most experiments and analyses under the supervision of Y. K. H. S. and M. F. measured densities and surface properties. M. F. and K. K. conducted MD simulations under the supervision of N. M. M. F. mainly wrote the manuscript with contributions and discussions from all authors, especially Y. K.

Conflicts of interest

There are no conflicts to declare.

Data availability

The data supporting this article have been included as part of the supplementary information (SI). Supplementary information: Tables S1–S6 and further figures for analysis (Fig. S1–S4). See DOI: https://doi.org/10.1039/d6sm00321d.

Acknowledgements

This work is partially supported by JSPS KAKENHI Grant Number JP22H0204.

References

1 J. N. A. Canongia Lopes and A. A. H. Pádua, *J. Phys. Chem. B*, 2006, **110**, 3330–3335.
2 A. Triolo, O. Russina, H.-J. Bleif and E. Di Cola, *J. Phys. Chem. B*, 2007, **111**, 4641–4644.
3 Y. L. Wang, B. Li, S. Sarman, F. Mocci, Z. Y. Lu, J. Yuan, A. Laaksonen and M. D. Fayer, *Chem. Rev.*, 2020, **120**, 5798–5877.
4 A. W. Taylor, P. Licence and A. P. Abbott, *Phys. Chem. Chem. Phys.*, 2011, **13**, 10147–10154.
5 A. Kaintz, G. Baker, A. Benesi and M. Maroncelli, *J. Phys. Chem. B*, 2013, **117**, 11697–11708.
6 Y. Kimura, Y. Kida, Y. Matsushita, Y. Yasaka, M. Ueno and K. Takahashi, *J. Phys. Chem. B*, 2015, **119**, 8096–8103.
7 S. Nakajima, H. Sumida, T. Endo and Y. Kimura, *Bull. Chem. Soc. Jpn.*, 2022, **95**, 1220–1227.

8 M. Fujiwara, S. Okazoe, S. Suzuki, K. Osawa, T. Endo and Y. Kimura, *Phys. Chem. Chem. Phys.*, 2026, **28**, 8949–8957.
9 T. Iwahashi, T. Ishiyama, Y. Sakai, A. Morita, D. Kim and Y. Ouchi, *Phys. Chem. Chem. Phys.*, 2020, **22**, 12565–12576.
10 T. Iwahashi, D. Kim and Y. Ouchi, *J. Chem. Phys.*, 2025, **162**, 014705.
11 M. Mezger, H. Schröder, H. Reichert, S. Schramm, J. S. Okasinski, S. Schöder, V. Honkimäki, M. Deutsch, B. M. Ocko, J. Ralston, M. Rohwerder, M. Stratmann and H. Dosch, *Science*, 2008, **322**, 424–428.
12 N. Nishi, J. Uchiyashiki, T. Oda, M. Hino and N. L. Yamada, *Bull. Chem. Soc. Jpn.*, 2021, **94**, 2914–2918.
13 K. Shimada and Y. Kimura, *J. Mol. Liq.*, 2023, **391**, 123269.
14 S. Singh, *Handbook of Liquid Crystals, Foundations and Fundamental Aspects*, Springer, 2025, vol. 1.
15 S. Singh, *Handbook of Liquid Crystals, Advanced Aspects and Applications*, Springer, 2025, vol. 1.
16 H. K. Bisoyi and Q. Li, *Chem. Rev.*, 2022, **122**, 4887–4926.
17 K. Goossens, K. Lava, C. W. Bielawski and K. Binnemans, *Chem. Rev.*, 2016, **116**, 4643–4807.
18 S. V. Dvinskikh, *Liq. Cryst.*, 2020, **47**, 1975–1985.
19 S. Miyajima, N. Nakamura and H. Chihara, *Bull. Chem. Soc. Jpn.*, 1983, **56**, 400–404.
20 M. Hara, H. Takezoe and A. Fukuda, *Jpn. J. Appl. Phys.*, 1986, **25**, 1756–1761.
21 J. E. Hallett, D. W. Hayward, T. Arnold, P. Bartlett and R. M. Richardson, *Soft Matter*, 2017, **13**, 5535–5542.
22 M. Sadati, H. Ramezani-Dakhel, W. Bu, E. Sevgen, Z. Liang, C. Erol, M. Rahimi, N. Taheri Qazvini, B. Lin, N. L. Abbott, B. T. Roux, M. L. Schlossman and J. J. de Pablo, *J. Am. Chem. Soc.*, 2017, **139**, 3841–3850.
23 K. Koevar and I. Muevi, *Liq. Cryst.*, 2001, **28**, 599–606.
24 S. Chakraborty, N. Nelson and D. K. Schwartz, *Soft Matter*, 2015, **11**, 7712–7716.
25 J. K. Srivastava, R. K. Singh, R. Dhar and S. Singh, *RSC Adv.*, 2015, **5**, 86291–86302.
26 K. Dan, A. Datta, Y. Yoshida, G. Saito, K. Yoshikawa and M. Roy, *J. Chem. Phys.*, 2016, **144**, 084904.
27 A. Datta, K. Yoshikawa, Y. Yoshida and G. Saito, *Front. Phys.*, 2020, **8**, 583173.
28 M. Terazima, *Bull. Chem. Soc. Jpn.*, 2023, **96**, 852–871.
29 M. Terazima, Y. Kojima and N. Hirota, *Chem. Phys. Lett.*, 1996, **259**, 451–458.
30 N. Nakajima, N. Hirota and M. Terazima, *J. Photochem. Photobiol., A*, 1999, **120**, 1–9.
31 M. Kondoh, H. Moritani and T. Ishibashi, *Bull. Chem. Soc. Jpn.*, 2020, **93**, 671–675.
32 Y. Kimura, S. Ibaraki, R. Hirano, Y. Sugita, Y. Yasaka and M. Ueno, *Phys. Chem. Chem. Phys.*, 2017, **19**, 22161–22168.
33 M. Ando, M. Koyakkat, T. Ueda, T. Minato and H. Shirota, *Langmuir*, 2023, **39**, 12090–12098.
34 M. J. Frisch, G. W. Trucks, H. B. Schlegel, G. E. Scuseria, M. A. Robb, J. R. Cheeseman, G. Scalmani, V. Barone, G. A. Petersson, H. Nakatsuji, X. Li, M. Caricato, A. V. Marenich, J. Bloino, B. G. Janesko, R. Gomperts, B. Mennucci, H. P. Hratchian, J. V. Ortiz, A. F. Izmaylov, J. L. Sonnenberg, D. Williams-Young, F. Ding, F. Lipparini, F. Egidi, J. Goings, B. Peng, A. Petrone, T. Henderson, D. Ranasinghe, V. G. Zakrzewski, J. Gao, N. Rega, G. Zheng, W. Liang, M. Hada, M. Ehara, K. Toyota, R. Fukuda, J. Hasegawa, M. Ishida, T. Nakajima, Y. Honda, O. Kitao, H. Nakai, T. Vreven, K. Throssell, J. A. Montgomery Jr., J. E. Peralta, F. Ogliaro, M. J. Bearpark, J. J. Heyd, E. N. Brothers, K. N. Kudin, V. N. Staroverov, T. A. Keith, R. Kobayashi, J. Normand, K. Raghavachari, A. P. Rendell, J. C. Burant, S. S. Iyengar, J. Tomasi, M. Cossi, J. M. Millam, M. Klene, C. Adamo, R. Cammi, J. W. Ochterski, R. L. Martin, K. Morokuma, O. Farkas, J. B. Foresman and D. J. Fox, Gaussian 16, 2016.
35 W. L. Jorgensen and J. Tirado-Rives, *Proc. Natl. Acad. Sci. U. S. A.*, 2005, **102**, 6665–6670.
36 L. S. Dodda, J. Z. Vilseck, J. Tirado-Rives and W. L. Jorgensen, *J. Phys. Chem. B*, 2017, **121**, 3864–3870.
37 L. S. Dodda, I. Cabeza de Vaca, J. Tirado-Rives and W. L. Jorgensen, *Nucleic Acids Res.*, 2017, **45**, W331–W336.
38 C. I. Bayly, P. Cieplak, W. Cornell and P. A. Kollman, *J. Phys. Chem.*, 1993, **97**, 10269–10280.
39 D. A. Case, H. M. Aktulga, K. Belfon, D. S. Cerutti, G. A. Cisneros, V. W. D. Cruzeiro, N. Forouzesh, T. J. Giese, A. W. Götz, H. Gohlke, S. Izadi, K. Kasavajhala, M. C. Kaymak, E. King, T. Kurtzman, T.-S. Lee, P. Li, J. Liu, T. Luchko, R. Luo, M. Manathunga, M. R. Machado, H. M. Nguyen, K. A. O'Hearn, A. V. Onufriev, F. Pan, S. Pantano, R. Qi, A. Rahnamoun, A. Risheh, S. Schott-Verdugo, A. Shajan, J. Swails, J. Wang, H. Wei, X. Wu, Y. Wu, S. Zhang, S. Zhao, Q. Zhu, T. E. Cheatham, III, D. R. Roe, A. Roitberg, C. Simmerling, D. M. York, M. C. Nagan and K. M. Merz, Jr., *J. Chem. Inf. Model.*, 2023, **63**, 6183–6191.
40 L. Martínez, R. Andrade, E. G. Birgin and J. M. Martínez, *J. Comput. Chem.*, 2009, **30**, 2157–2164.
41 M. J. Abraham, T. Murtola, R. Schulz, S. Páll, J. C. Smith, B. Hess and E. Lindahl, *SoftwareX*, 2015, **1–2**, 19–25.
42 K. Kasahara, ANATRA, https://github.com/kenkasa/anatra.
43 C. Kolbeck, J. Lehmann, K. R. J. Lovelock, T. Cremer, N. Paape, P. Wasserscheid, A. P. Fröba, F. Maier and H. P. Steinrück, *J. Phys. Chem. B*, 2010, **114**, 17025–17036.
44 L. Xue, E. Gurung, G. Tamas, Y. P. Koh, M. Shadeck, S. L. Simon, M. Maroncelli and E. L. Quitevis, *J. Chem. Eng. Data*, 2016, **61**, 1078–1091.
45 L. Alonso, A. Arce, M. Francisco and A. Soto, *J. Chem. Eng. Data*, 2008, **53**, 1750–1755.
46 N. Hazrati, M. Abdouss, A. A. Miran Beigi, A. A. Pasban and M. Rezaei, *J. Chem. Eng. Data*, 2017, **62**, 3084–3094.
47 I. Yeh and G. Hummer, *J. Phys. Chem. B*, 2004, **108**, 15873–15879.
48 W. Ochędzan-Siodłak, K. Dziubek and D. Siodłak, *J. Mol. Liq.*, 2013, **177**, 85–93.
49 A. Aljasmi, A. S. AlJimaz, K. H. A. E. AlKhaldi and A. A. Mohammad, *J. Chem. Eng. Data*, 2024, **69**, 1564–1577.
50 O. Russina, A. Triolo, L. Gontrani, R. Caminiti, D. Xiao, L. G. Hines, R. A. Bartsch, E. L. Quitevis, N. Plechkova and K. R. Seddon, *J. Phys.: Condens. Matter*, 2009, **21**, 424121.

51 S. Tsuzuki, W. Shinoda, H. Saito, M. Mikami, H. Tokuda and M. Watanabe, *J. Phys. Chem. B*, 2009, **113**, 10641–10649.
52 D. Bedrov, J.-P. Piquemal, O. Borodin, A. D. MacKerell Jr., B. Roux and C. Schröder, *Chem. Rev.*, 2019, **119**, 7940–7995.
53 R. Kusaka, S. Nihonyanagi and T. Tahara, *Nat. Chem.*, 2021, **13**, 306–311.
54 K. Matsuzaki, R. Kusaka, S. Nihonyanagi, S. Yamaguchi, T. Nagata and T. Tahara, *J. Am. Chem. Soc.*, 2016, **138**, 7551–7557.
55 T. Yamashita, T. Uchida, T. Fukushima and N. Teramae, *J. Phys. Chem. B*, 2003, **107**, 4786–4792.
56 K. Nakatani, S. Ishizaka and N. Kitamura, *Anal. Sci.*, 1996, **12**, 701–705.

